Nonlinear harmonics of a seeded free-electron laser as a coherent and ultrafast probe to investigate matter at the water window and beyond

G. Penco, G. Perosa, E. Allaria, L. Badano, F. Bencivenga, A. Brynes, C. Callegari, F. Capotondi, A. Caretta, P. Cinquegrana, et al.

Nonlinear harmonics of a seeded free-electron laser as a coherent and ultrafast probe to investigate matter at the water window and beyond

G. Penco[1,*] G. Perosa,[2] E. Allaria,[1,3] L. Badano,[1] F. Bencivenga,[1] A. Brynes,[1] C. Callegari,[1] F. Capotondi,[1] A. Caretta,[1] P. Cinquegrana,[1] S. Dal Zilio,[4] M. B. Danailov,[1] D. De Angelis,[1] A. Demidovich,[1] S. Di Mitri,[1,2] L. Foglia,[1] G. Gaio,[1] A. Gessini,[1] L. Giannessi,[1,5] G. Kurdi,[1] M. Manfredda,[1] M. Malvestuto,[1] C. Masciovecchio,[1] R. Mincigrucci,[1] I. Nikolov,[1] E. Pedersoli,[1] S. Pelli Cresi,[1] E. Principi,[1] P. Rebernik,[1] A. Simoncig,[1] S. Spampinati,[1] C. Spezzani,[1] F. Sottocorona,[2] M. Trovó,[1] M. Zangrando,[1,4] V. Chardonnet,[6] M. Hennes,[6] J. Lüning,[6,†] B. Vodungbo,[6] P. Bougiatioti,[7] C. David,[7] B. Roesner,[7] M. Sacchi,[8] E. Roussel,[9] E. Jal,[6] and G. De Ninno[1,10,‡]

[1]*Elettra-Sincrotrone Trieste S.C.p.A., 34149 Trieste, Italy*
[2]*Dipartimento di Fisica, Università degli Studi di Trieste, Piazzale Europa 1, 34127 Trieste, Italy*
[3]*Deutsches Elektronen-Synchrotron, 22607 Hamburg, Germany*
[4]*Istituto Officina dei Materiali, Consiglio Nazionale delle Ricerche, 34149 Trieste, Italy*
[5]*Laboratori Nazionali di Frascati, INFN, Via Enrico Fermi 54, 00044 Frascati, Italy*
[6]*Sorbonne Université, CNRS, Laboratoire de Chimie Physique-Matière et Rayonnement, LCPMR, Paris 75005, France*
[7]*Paul Scherrer Institut, 5232 Villigen, Switzerland*
[8]*Institut des NanoSciences de Paris, UMR 7588, CNRS, Sorbonne Université, 75005 Paris, France and Synchrotron SOLEIL, L'Orme des Merisiers, Saint-Aubin, BP 48, 91192 Gif-sur-Yvette, France*
[9]*Univ. Lille, CNRS, UMR 8523 - PhLAM - Physique des Lasers Atomes et Molécules, F-59000 Lille, France*
[10]*Laboratory of Quantum Optics, University of Nova Gorica, 5001 Nova Gorica, Slovenia*

(Received 29 November 2021; revised 18 April 2022; accepted 20 April 2022; published 26 May 2022)

The advent of free-electron lasers (FELs) in the soft- and hard-x-ray spectral regions has introduced the possibility to probe electronic, magnetic, and structural dynamics, in both diluted and condensed matter samples, with femtosecond time resolution. In particular, FELs have strongly enhanced the capabilities of several analytical techniques, which have taken advantage of the high degree of transverse coherence provided. Free-electron lasers based on the harmonic up-conversion of an external coherent source (seed) are characterized also by a high degree of longitudinal coherence, since electrons inherit the coherence properties of the seed. For the state of the art, the shortest wavelength delivered to user experiments by an externally seeded FEL light source is about 4 nm. In this paper we demonstrate that pulses with a high longitudinal degree of coherence (first and second order) covering the water window and with photon energy extending up to 790 eV can be generated by exploiting the so-called nonlinear harmonic regime, which allows generation of radiation at harmonics of the resonant FEL wavelength. In order to show the suitability of the nonlinear harmonics generated by a seeded FEL for research in the water window and beyond, we report the results of two proof-of-principle experiments: one measuring the oxygen K-edge absorption in water (∼530 eV) and the other analyzing the spin dynamics of Fe and Co through magnetic small-angle x-ray scattering at their L edges (707 and 780 eV, respectively).

DOI: 10.1103/PhysRevA.105.053524

I. INTRODUCTION

The scientific challenge of tracking the temporal evolution of an excited state of matter after an external stimulus, on the atomic scale and with elemental sensitivity, has boosted the evolution of powerful free-electron laser (FEL) sources in the extreme ultraviolet (EUV) and soft- or hard-x-ray ranges [1]. Several techniques, including Fourier transform holography, coherent diffraction imaging, and ptychography, exploit the high degree of transverse coherence of the FEL pulses and, in the case of seeded FELs, of longitudinal coherence. The latter is of paramount importance for techniques, such as linear and nonlinear spectroscopies and coherent control, which require both phase and wavelength manipulation within a given pulse. In a seeded FEL operated in the so-called high-gain harmonic generation (HGHG) regime [2], an external coherent source (a laser) is used to imprint an energy modulation on an ultrarelativistic electron beam passing through an undulator, known as the modulator. In a planar undulator, the latter is tuned to satisfy the resonant condition [3]

$$\lambda_S = \frac{\lambda_u(1 + K^2/2)}{2\gamma^2}, \tag{1}$$

where λ_S is the seed wavelength, λ_u is the undulator period, $K = \frac{eB_u\lambda_u}{2\pi m_e c}$ is the normalized undulator strength, m_e is

*giuseppe.penco@elettra.eu
†Present address: Helmholtz-Zentrum Berlin für Materialien und Energie, 14109 Berlin, Germany.
‡giovanni.deninno@elettra.eu

the electron rest mass, c is the speed of light in vacuum, B_u is the peak magnetic field, and γ is the Lorentz factor. The electron bunch is then sent through a magnetic dispersive section that converts the energy modulation into density modulation, called bunching, whose spectral content includes, with progressively fading coefficients, higher harmonics of the seed. The bunched electrons are then injected into an undulator, which is tuned to be resonant to a given harmonic of the seed wavelength λ_n, with integer n [4]. Since the emission process is stimulated by the seed, all electrons emit in phase. Phase-locked emission results in the generation of near Fourier-transform-limited pulses at λ_n [5,6].

The fading of the bunching with increasing n sets a limit to the shortest wavelength that can be generated using this method [7]. Indeed, the bunching level at the desired harmonic must be significantly larger than the shot noise; otherwise a competitive amplification process, namely, self-amplified spontaneous emission (SASE) [8–10], may become dominant and spoil the longitudinal coherence of the output radiation. Recently, a cold electron beam with very low slice energy spread has been demonstrated at FERMI [11], leading to the extension of the limit of the harmonic upshift conversion in a single HGHG stage, and FEL gain was observed up to harmonic 25 (of a seed in the UV range).

For reliable operation at shorter wavelengths down to the soft-x-ray range, the HGHG scheme has been implemented in a two-stage configuration, using the emission of the first stage to seed the second one. The state-of-the-art shortest wavelength delivered to users is about 4 nm [12–14], corresponding to harmonic 65 [15,16] of an UV laser. A recent experiment has demonstrated that a similar wavelength range can be achieved in a single stage using the echo-enabled harmonic generation (EEHG) technique [17,18]. Adopting the EEHG scheme, stable and narrowband coherent pulses at 2.6 nm (∼474 eV), i.e., harmonic 101, were generated, even though the parameters used for the experiment allowed only a weak intensity, comparable to the broadband spontaneous emission coming from the whole electron beam [19]. A few options for further extending the range of an externally seeded FEL toward 2 nm have been studied but not yet implemented [20–22].

Strong scientific cases exist for developing sources that deliver fully coherent and variable-polarization ultrashort photon pulses over the spectral region that covers the water window (up to the O K edge at 530 eV) and the L edges of the 3d transition metals up to 800 eV [23–27]. The availability of such sources would make it possible to address the dynamics of organic molecules in solution and to investigate the electronic excitations in strongly correlated materials via pump-probe experiments at different core resonances, with both site and chemical sensitivity.

In this paper we demonstrate that light pulses with the above-mentioned properties can be generated by operating a seeded FEL in the so-called nonlinear harmonic generation (NHG) regime [28–31]. In this regime, the exponential gain leading to the generation of the harmonic λ_n drives the bunching, and consequent emission, at λ_n/m, where m is an integer. Nonlinear harmonic generation has been proposed in the past as a way to extend the tuning range to short wavelengths not reachable by the electron-beam and undulator parameters at the fundamental [32–34]: Numerical simulations estimated intensity ratios between the third and fifth nonlinear harmonics and the fundamental of about 2% and 0.3%, respectively.

An alternative to the NHG technique is represented by the harmonic lasing (HL) regime [35–37], where the electron interaction with the fundamental is disrupted while an odd higher harmonic is allowed to evolve unhindered. For a large undulator K parameter ($\gtrapprox 2$), HL allows a gain length at the harmonic comparable to the one at the fundamental, enabling the transfer of most of the energy lost by the electrons to the harmonic field [37,38]. For a smaller K parameter (close to 1), as is the case of the FERMI FEL spectral range described below, the gain length at the harmonic is too large and bunching amplification through NHG proves more efficient.

We present a detailed description of the process leading to optimized nonlinear harmonic emission in the water window and beyond, as well as the characterization of the generated pulses in terms of spectral purity, pulse energy, and longitudinal coherence. In this spectral domain, more powerful FEL pulses can be provided by SASE operation but at the cost of longitudinal coherence and spectral quality: Typically, the relative bandwidth of SASE in the soft x ray is of the order of 0.2%–0.5% at the fundamental resonant wavelength [39]. Operating the FEL in the self-seeding mode [40] allows a reduction of the bandwidth with an improvement of the longitudinal coherence, but it does not suppress the stochastic nature of the process, because it inherits the poor longitudinal coherence of the SASE FEL, from which it originates [41,42].

We show that under properly optimized conditions a very high wavelength stability (a few 10^{-4}) and a spectral bandwidth smaller than 0.1% at 790 eV can be achieved, combined with a high degree of longitudinal coherence, very similar to what is usually obtained when the FEL is operated at the fundamental wavelength. In particular, we show that the high degree of longitudinal coherence, which is imparted by the seed to the light at λ_n in the linear regime, extends to the nonlinear harmonic λ_n/m.

To demonstrate that nonlinear harmonics generated by a seeded FEL can be profitably used to perform experiments on matter, we report the results of two proof-of-principle studies. In the first one, the absorption spectrum of room-temperature water has been measured, across the oxygen K edge (530–550 eV). The second experiment studied the magnetization dynamics of thin films at the Co and Fe L edges, i.e., 702–716 and 771–785 eV, respectively, through small-angle x-ray scattering. The successful operation of FERMI at this energy is relevant, e.g., for studies of ultrafast spin dynamics [43,44] and for spectroscopy applications in biological systems [45].

II. EXPERIMENTAL CHARACTERIZATION OF SEEDED FEL PULSES AT 700–780 AND 530 eV

The experiment was carried out at FERMI [16], a seeded HGHG FEL user facility. FERMI has two FEL lines: FEL-1, consisting of a single HGHG stage covering the spectral range from 100 to 20 nm [46], and FEL-2 [15], from 20 to 4 nm, whose layout is sketched in Fig. 1. FEL-2 is based on two HGHG stages with an interposed magnetic chicane (DL) to control the delay between the electrons and the emission of the first stage. In this way, the latter seeds a "fresh" portion

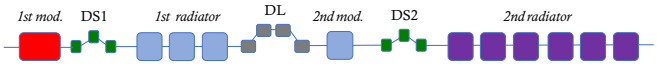

FIG. 1. FERMI FEL-2 layout, including the two dispersive sections (DS1 and DS2) and a delay line (DL) in between the two stages for the operation in fresh-bunch mode.

of the electron bunch, not spoiled by the FEL process that took place in the first stage; this is technically known as the fresh-bunch mode [47]. The electron bunch is then sent along a second undulator chain (second radiator in Fig. 1) tuned to a harmonic of the first stage. A large flexibility in tuning the final wavelength is provided by the APPLE-II undulators [48] that feature a variable gap and selectable polarization (circular, linear horizontal, and linear vertical) [49]. We focused our attention on the properties of the third nonlinear harmonic and we set the fundamental wavelength in linear horizontal polarization. In this configuration, the harmonic radiation is emitted along the electron propagation axis [50–52].

In the following section we report on the generation of the third nonlinear harmonic of ∼233 eV (i.e., 5.3 nm), corresponding to ∼700 eV. A comparable performance was obtained at the Fe L edge (∼710 eV) and at the Co L edge (∼780 eV).

In order to characterize simultaneously the FEL emission at both the fundamental (233 eV) and third nonlinear harmonic wavelength (700 eV) on a shot-to-shot basis, we used two high-resolution spectrometers placed in series (Fig. 2) one (PRESTO) [53] integrated in the common photon transport line [54] of the FERMI experimental hall, the other (WEST) recently installed downstream of the EIS-TIMEX end station [55].

The growth of the FEL intensity at 233 eV and at 700 eV along the undulator chain has been measured from the integrated signal of the PRESTO and WEST spectrometers, respectively, and is reported in Fig. 3. Numerical simulations have been run with GENESIS 1.3 [56] using the beam parameters listed in Table I, representing the experimental condition. The obtained results are reported in Fig. 3. In order to compare the simulation and the experimental results, the latter were scaled according to the pulse energy estimation reported in the following (i.e., 19.4 μJ per pulse at 233 eV and 150 nJ per pulse at 700 eV).

The simulations are in good agreement with the measurements in describing the FEL gain of the fundamental and of the third harmonic. The harmonic growth results in fact from the sum of a linear and a nonlinear contribution. The former

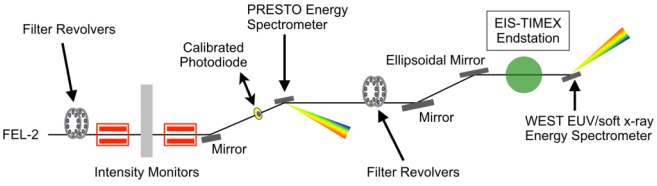

FIG. 2. Sketch of the photon transport line, including the intensity monitors, the filter revolvers, the calibrated photodiode, and the two spectrometers (PRESTO [53] and WEST [55]) used in the experiment.

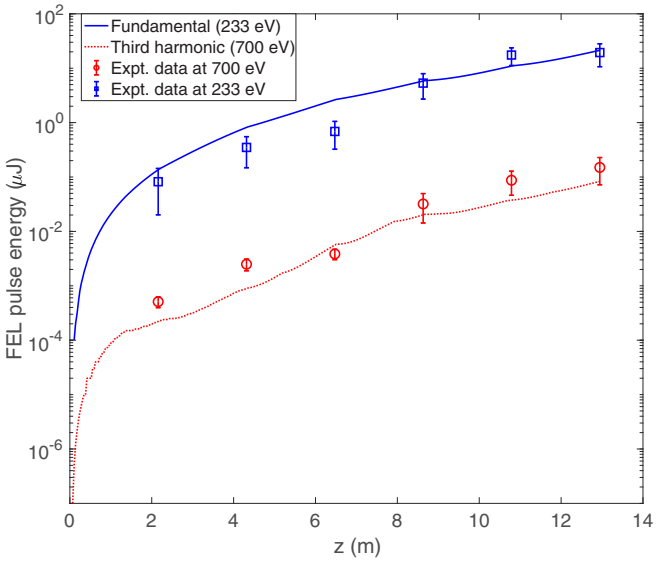

FIG. 3. Measured (markers) and simulated (lines) FEL gain curves at 233 eV (i.e., 5.3 nm) and at 700 eV (i.e., 1.77 nm). The measurements were done by progressively detuning the undulator gap of the second-stage radiator and by integrating the spectra on PRESTO (for 233 eV) and on WEST (for 700 eV) within a narrow bandwidth around the central wavelength. Error bars correspond to the standard deviation from the mean value calculated over 50 shots.

dominates in the first part of the radiator, where as a result of the seeding there is a non-negligible bunching also at the harmonic of the resonant wavelength. When the fundamental field grows along the radiator, it contributes to the increase of the electron bunching at its harmonics, entering in a nonlinear regime and sustaining the harmonic gain. Simulations via GENESIS confirmed the important contribution to the harmonic gain coming from the fundamental growth, showing that if the latter is artificially suppressed in the simulation, the harmonic field is depleted by about 50%.

In order to estimate the spectral quality of the emitted radiation, a series of 400 consecutive single-shot spectra at 700 eV are analyzed (Fig. 4). The FEL had a shot-to-shot power stability of about 20%, retrieved from the spectral intensity [see Fig. 4(c)], and a central wavelength stability of 0.03% (rms) [Fig. 4(b)]. The statistics over the FEL bandwidth [Fig. 4(d)] reveal that the largest fraction of shots have a relative FWHM bandwidth smaller than 0.1%. Spectral sidebands and associated fluctuations of the pulse bandwidth, with values down to 3×10^{-4} (the PRESTO spectrometer resolution is about 5×10^{-5}), can be partially associated with

TABLE I. Main electron-beam parameters during the experiment and used in the simulations.

Parameter	Value	Unit
beam energy	1.48	GeV
peak current	670	A
slice energy spread	60	keV
slice normalized emittance	1.4	mm mrad
average Twiss β function	7.5	m

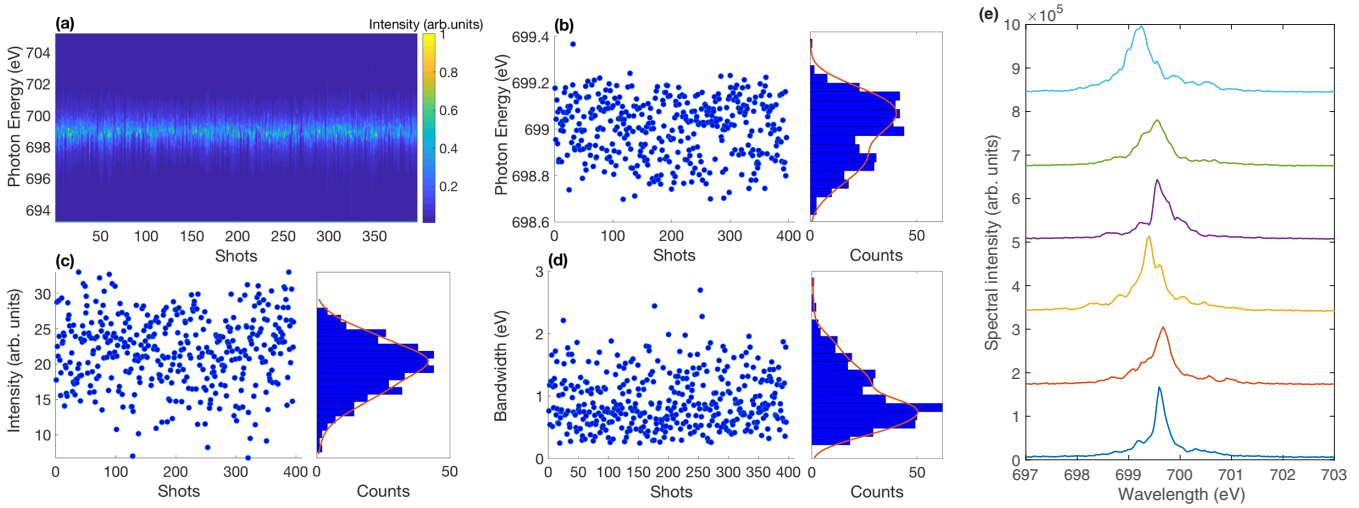

FIG. 4. (a) Series of 400 consecutive single-shot spectra at 700 eV acquired with the PRESTO spectrometer. Also shown are the statistics of (b) the central wavelength stability, (c) the spectral intensity, and (d) the FWHM spectral bandwidth. (e) Random sample of the single-shot spectra.

microbunching instabilities (MBI). These instabilities are due to the collective interaction of charged particles in the accelerator, in which small initial variations in the energy or longitudinal density of the particles can be amplified during the acceleration process, ultimately deteriorating the spectral quality of the light produced by a seeded FEL. Numerical simulations using a 100-fs seed laser and an electron beam devoid of MBI foresee an unstructured FEL pulse with a relative FWHM bandwidth of a few 10^{-4} (corresponding to an ∼25-fs pulse at the Fourier limit). On the contrary, the random series of single-shot spectra in Fig. 4(e) show sideband structures that may be attributed to the presence of MBI. A common method to suppress MBI uses a laser-heater system [57] that induces a controlled increase of the electron slice energy spread at the injector exit (at around 100 MeV electron-beam energy). This damps the microbunching growth occurring along the linac and in the dispersive regions, such as bunch compressors and the spreader [58]. The laser-heater power has been demonstrated to be a key parameter to maximize the FEL intensity [59]. In these conditions, residual microbunching structures (at wavelengths of about 1 μm) can survive. These incoherent modulations sum in frequency with the FEL emission, deteriorating the spectrum with lateral sidebands and increasing the emission bandwidth [see Fig. 4(e)] [60]. To study the effects of MBI, we have therefore scanned the intensity of the laser heater and measured the FEL spectra at 700 eV (results reported in Fig. 5). The statistics shown in Fig. 4 refer to a laser-heater pulse energy of about 1 μJ and correspond to the maximum FEL intensity and to an average FWHM bandwidth of about 1.2 eV. By increasing the laser-heater energy beyond this value, the FEL intensity decreases because of the larger slice energy spread (i.e., lower FEL gain), but the larger damping of the MBI further improves the spectral purity and the FEL bandwidth visibly narrows. At a trade-off laser-heater energy of ∼2.7 μJ, the average FEL bandwidth is reduced to about 0.6 eV (i.e., to a spectral purity $\Delta E/E \sim 8 \times 10^{-4}$) [Fig. 5(c)] at the cost of a factor 2 reduction in the FEL energy per pulse. A significant fraction of the shots (about 20%) exhibit a spectral bandwidth as narrow as 0.4 eV (5×10^{-4}), approaching the ideal case in agreement with numerical simulations. A further advantage provided by the increase in laser-heater power is represented by a factor 2 reduction of intensity fluctuations [see Fig. 5(a)].

To estimate the pulse energy of the output radiation, we used a calibrated photodiode (see Fig. 2) and a set of solid-state filters to minimize contributions from undesired radiation (i.e., the seed laser and the emission from the first stage of FEL-2). Since the calibrated photodiode is an invasive diagnostic, it did not allow us to measure simultaneously the spectrum of the fundamental and of the third nonlinear harmonic as shown in Fig. 3 and to retrieve from a calibrated spectral area the absolute value of the emitted pulse energy. However, inserting different kinds of solid-state filters with known transmission curves made it possible to estimate the pulse energy at 700 and 233 eV. Details on this procedure are reported in Appendix A. The average pulse energies at the fundamental emission wavelength (233 eV) and at the nonlinear third harmonic (700 eV) were estimated to be 19.4 μJ (with a rms uncertainty of 0.1 μJ) and 150 nJ (with a rms uncertainty of 100 nJ), respectively. The derived estimation is indeed in good agreement with the 1:100 ratio between the pulse energy of the third nonlinear harmonic and that of the fundamental, as expected from the simulation.

We collected a second set of data at the oxygen K edge, at about 530 eV (i.e., 2.33 nm), corresponding to the third harmonic of 177 eV (i.e., 7.0 nm). The data reported in Fig. 6 show a spectral intensity jitter of about 25% (rms) and a central wavelength jitter of about 8×10^{-5} (rms). A large fraction of shots, about 50%, have a spectral FWHM bandwidth of less than 0.4 eV ($\sim 7 \times 10^{-4}$).

We estimated a pulse energy at 7 nm at the source of about 18 μJ. As in the previous case, exploiting a combination of

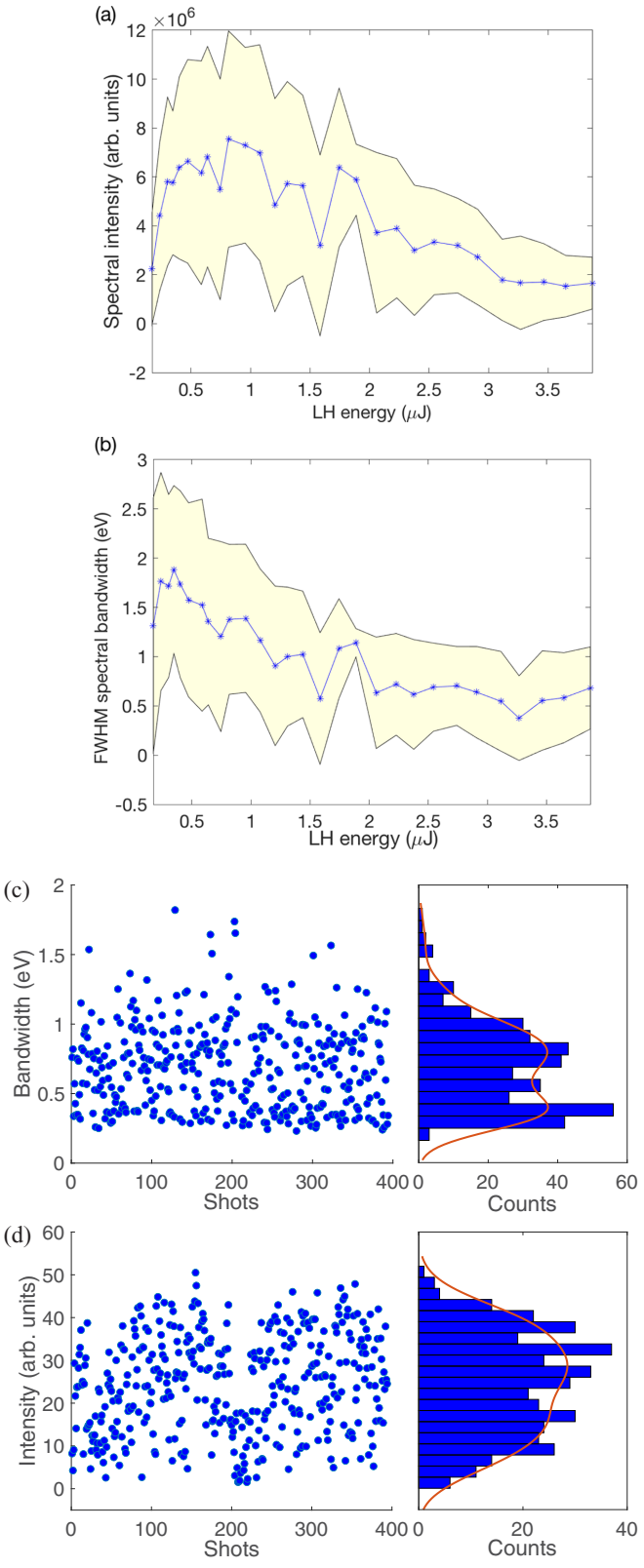

FIG. 5. (a) Spectral intensity and (b) FWHM bandwidth as functions of the laser-heater pulse energy at 700 eV. Also shown are the statistics over 400 shots of (c) the spectral bandwidth and (d) the intensity for a laser-heater pulse energy of 2.7 μJ. Shaded regions around the central blue curves in (a) and (b) represent the rms fluctuations of the FEL intensity and bandwidth, respectively, measured for each value of the laser-heater pulse energy.

filters, we estimated a pulse energy at 530 eV in the range 100–200 nJ at the source, that is, about 1% of the fundamental, similar to the results obtained at 700 eV.

Despite the lower fluence of the nonlinear harmonic compared to the fundamental, there are classes of experiments involving, e.g., the studies of spin dynamics that do not require high brightness and which are difficult to perform in standard slicing sources at synchrotron radiation facilities. Moreover, it has been demonstrated that even below the sample damage threshold, magnetic information is lost at both the M edge and L edge of transition metals when the deposited energy exceeds a few tens of mJ/cm^2 [23,25,61]. As described below, the average intensity of the FERMI FEL optimized in NHG at the sample allows us to reach a fluence of about 50 mJ/cm^2, which is well above the soft-x-ray magnetic damage threshold.

III. LONGITUDINAL COHERENCE

The statistical properties of the light emitted by a seeded FEL differ substantially from those of a SASE FEL source. A SASE FEL has the typical statistics of chaotic light [62], while it was demonstrated that the harmonic conversion and amplification processes preserve part of the coherence properties of the seed laser, even at high harmonic orders, and the seeded FEL statistics resemble those of laser light [63]. The natural question is what happens to the light statistics of the nonlinear harmonics emitted at very short wavelengths by a seeded FEL and what is the second-order degree of coherence of this spectral component of the emitted light. Theoretical studies predict that the frequency multiplication process produces phase noise degradation proportional at least to the square of the frequency multiplication factor [64], preventing full coherence with a HGHG FEL at a very short-wavelength range. We have used the statistics of the spectra acquired at 700 eV and at 530 eV to calculate the normalized second-order correlation function $g^{(2)}$, defined in [65],

$$g^{(2)}(\lambda_1,\lambda_2)=\frac{\langle I(\lambda_1)I(\lambda_2)\rangle}{\langle I(\lambda_1)\rangle\langle I(\lambda_2)\rangle}, \tag{2}$$

where $I(\lambda_1)$ and $I(\lambda_2)$ are spectral intensities at different wavelengths measured simultaneously and the angular brackets indicate averaging over a large ensemble of different radiation pulses. In the literature, it is very common to represent $g^{(2)}$ as a function of $\Delta\lambda=\lambda_1-\lambda_2$. The value of $g^{(2)}(\Delta\lambda=0)$, generally indicated as $g^{(2)}(0)$, is a key parameter to define the degree of coherence of the radiation: it is 1 for a coherent source and 2 for chaotic light and assumes a value between 1 and 2 for partially coherent light [65–68]. Free-electron laser radiation generated in the SASE mode is characterized by $g^{(2)}(0)>1.5$ [66], while fully coherent sources like FERMI have been demonstrated to provide laser-like output, with a value of $g^{(2)}(0)$ close to 1 [63]. Routinely, we measure values of $g^{(2)}(0)$ between 1 and 1.2 and we ascribe the incoherent contribution to variations of machine and electron-beam parameters and residual contributions of spurious harmonic content in the beam (e.g., microbunching instability).

Figure 7 reports the $g^{(2)}$ function calculated for the spectra at 1.77 nm (i.e., 700 eV) and at 2.33 nm (i.e., 530 eV),

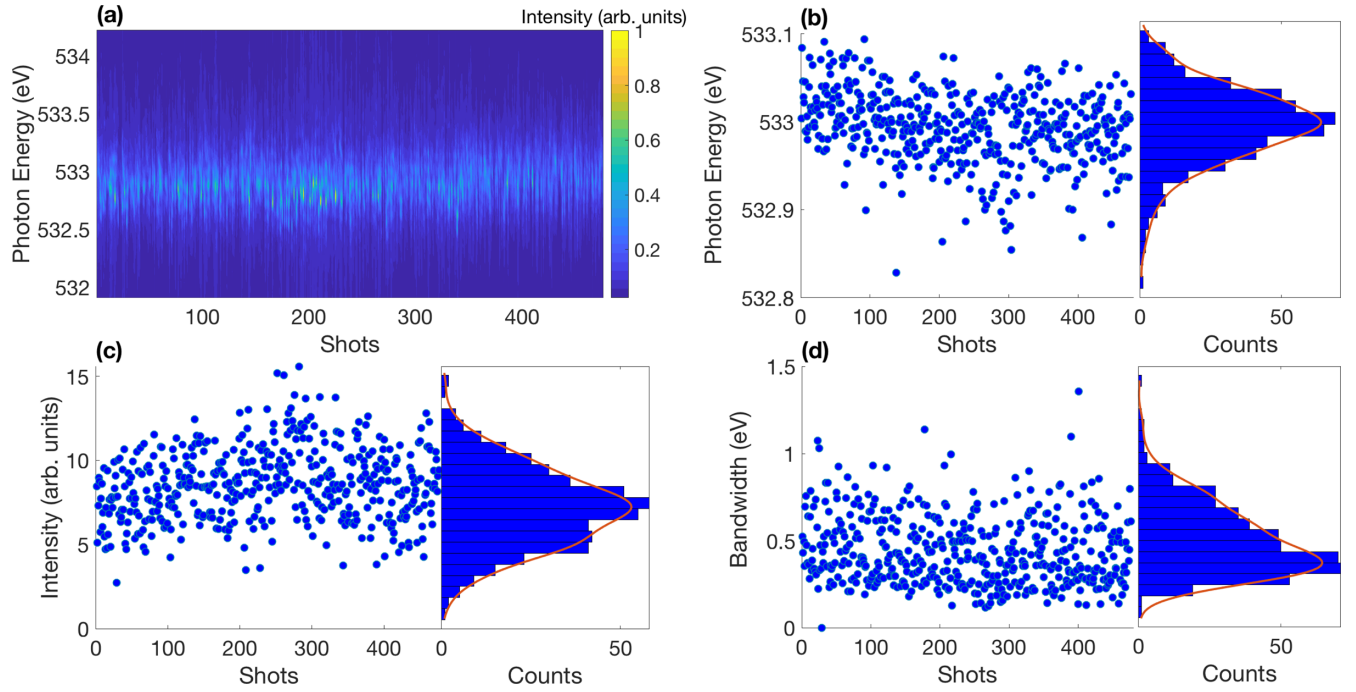

FIG. 6. (a) Series of 450 consecutive single-shot spectra at 533 eV (i.e., 2.33 nm) acquired with the PRESTO spectrometer. Also shown are the statistics about (b) the central wavelength stability, (c) the spectral intensity, and (d) the FWHM spectral bandwidth.

averaged over a very narrow central bandwidth ($\Delta\lambda = 3 \times 10^{-4}$ nm, green line) and a larger one ($\Delta\lambda = 1.5 \times 10^{-3}$ nm, blue line). The value of $g^{(2)}(0)$ ($\sim$1.16) is almost independent of the bandwidth chosen and in both cases the measured value is very close to the typical performance obtained at FERMI in the nominal spectral range (100–4 nm).

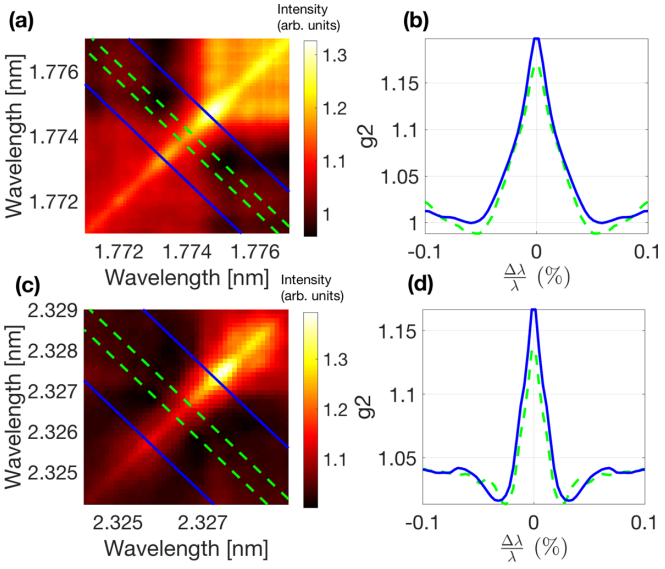

FIG. 7. Second-order spectral correlation function $g^{(2)}$ for 700 eV (1.77 nm) and 530 eV (2.33 nm) radiation: (a) and (c) the $g^{(2)}$ function calculated as defined in Eq. (2) for the two different photon energies and (b) and (d) the mean values of $g^{(2)}$ calculated averaging over a very narrow central bandwidth (green dotted line) and over a larger one (blue solid line).

IV. X-RAY-ABSORPTION SPECTROSCOPY OF WATER ACROSS THE OXYGEN *K* EDGE

The x-ray-absorption spectroscopy (XAS) spectrum of steady room-temperature water across the oxygen *K* edge ($\sim$535 eV) has been measured at the EIS-TIMEX beamline in the spectral region 530–545 eV (Fig. 8) operating in transmission geometry. The water sample was confined in a sealed microfluidic cell, with thin Si_3N_4 windows (100 nm thickness) transparent to the soft-x-ray radiation. The FEL beam was focused on the sample by an ellipsoidal mirror obtaining a spot of a few tens of microns, matching the cell window size.

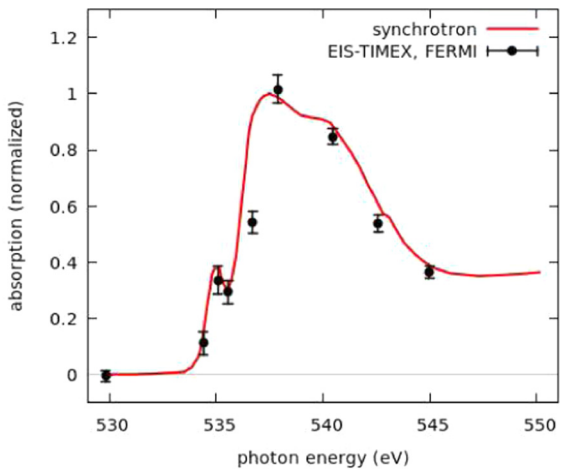

FIG. 8. Normalized XAS at the O *K* edge in transmission geometry of room-temperature water confined between Si_3N_4 windows as measured in this work (black closed circles). A similar measurement carried out at the SSRL synchrotron (red curve) [69] is shown for comparison.

The FEL photon energy was finely tuned to nine selected values (Fig. 8) using an optical parameter amplifier [70], but in principle a more refined scan around the oxygen K edge can be performed.

For each photon energy, the spectral line of the source was measured by integrating over 1500 FEL shots (30 s of acquisition for data point). These measurements were performed both with and without the sample, thus obtaining the total transmission of the sample and of the Si_3N_4 windows. The resulting XAS data, refined by applying preedge absorption linear background removal, are in good agreement with the XAS obtained at synchrotrons [69]. The narrow bandwidth and the high wavelength stability of the FERMI source at 530 eV permit the identification of typical features of the water spectrum, such as the prepeak around 535 eV (see Fig. 8), with a resolution better than 1 eV. This proof-of-principle experiment paves the way for light-driven subpicosecond dynamic studies in water and other molecules as well as in solid oxides by monitoring the time-resolved x-ray-absorption spectrum at the O K edge. Time-resolved XAS gives access to the ultrafast modifications of the electronic structure of oxygen across the Fermi level, revealing structural changes as well as charge transfer processes in oxygen-rich samples, triggered by exposure to light pulses.

V. PROBING SPIN DYNAMICS AT TRANSITION-METAL $L_{2,3}$ EDGES

In a second pilot experiment, the nonlinear harmonics produced by the seeded FEL were used in combination with an external optical pulse [71] to detect the spin dynamics occurring in transition-metal magnetic thin films. In particular, the FEL was tuned to generate photons across the Fe and Co $L_{2,3}$ edges, corresponding to the 702–716 eV (∼1.77 nm) and 771–785 eV (∼1.59 nm) ranges, respectively [25].

The measurements have been performed at the DiProI end-station of FERMI [72,73]. The beam was focused at the sample position to a large spot size of about 250 × 300 μm^2. An IR laser (780 nm wavelength, 100 fs FWHM pulse duration) focused onto a spot size of 350 × 400 μm^2 was used to excite uniformly the magnetic dynamics. A combination of Al and Zr filters was used to remove the spurious radiation generated by the source in the double-stage HGHG scheme.

Using a calibrated photodiode inside the experimental chamber, we estimate an average pulse energy of about 3 ± 2 nJ per pulse at the sample plane at both edges. This pulse energy, which includes all photon transport and focusing optics losses, is several orders of magnitude larger than that which is available with femtoslicing sources at third-generation synchrotrons [74,75].

The experimental setup, illustrated in Appendix B, was designed to collect time-dependent absorption and spin dynamics information of the magnetic sample. For the sake of simplicity, hereafter we will consider only the magnetic part of the experimental information, referring the reader to Appendix C for the XAS analysis. Static magnetic spectra of the two samples (FeTb alloy and CoPt multilayer) have been collected by scanning the FEL emission wavelength in an energy range across the Fe [Fig. 9(a)] and the Co [Fig. 9(b)] L_3 edge. These curves show the magnetic contribution without

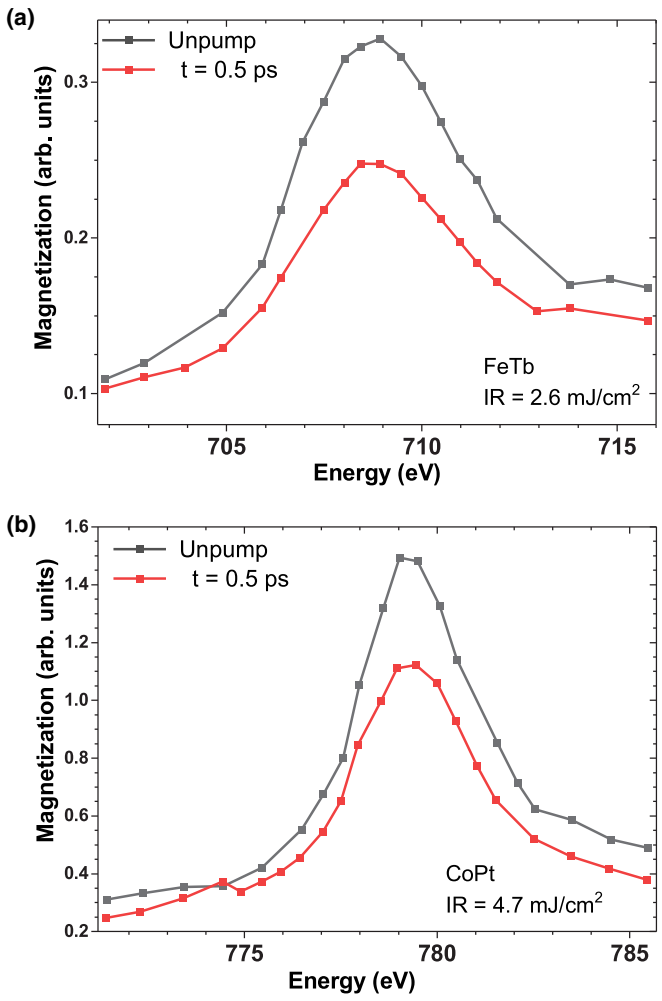

FIG. 9. Comparison of static (black squares) and optically pumped (probe delay of 0.5 ps, red squares) magnetic scattering efficiency for (a) a FeTb multilayer sample at the Fe L_3 edge and (b) a CoPt multilayer sample at the Co L_3 edge. Pump fluences are (a) 2.6 mJ/cm^2 for FeTb and (b) 4.7 mJ/cm^2 for CoPt.

(black) and 0.5 ps after (red) the sample excitation by the optical IR pump laser pulse. The experimental traces clearly show an increase of the magnetic scattering efficiency for the FeTb (CoPt) sample with a maximum at 709.2 eV (779.5 eV), corresponding to the L_3 resonance of Fe (Co). The same spectral traces obtained after 0.5 ps from pumping show a clear reduction of the magnetic scattering strength at the elemental resonance for both the FeTb and CoPt samples. Comparing the static XAS spectra (see Fig. 15 in Appendix B), with similar measurements performed at the SOLEIL synchrotron on the same sample, we estimate an energy resolution of about 0.8 eV, consistent with the average measured bandwidth reported in Fig. 4.

We have investigated the evolution of the magnetic scattering efficiency of both samples at a given probing photon energy (707 eV for FeTb and 778.5 eV for CoPt); the results are reported in Fig. 10. The data for the CoPt sample show that within 350 fs a minimum in the magnetic signal contrast is reached followed by a slow recovery to the unpumped state. Fitting the time-dependent demagnetization profile with

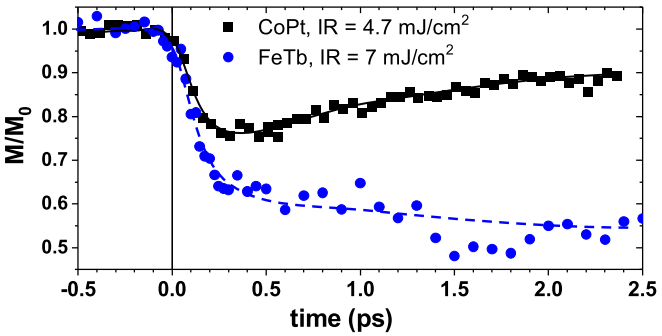

FIG. 10. Relative magnetic scattering efficiency as a function of the time delay for CoPt (778.5 eV, black squares) and FeTb strongly pumped (707.5 eV, blue circles).

an analytical function [76], a characteristic demagnetization time μ for Co species of about 120 ± 20 fs is extracted, in agreement with previously reported values [77,78]. A different behavior is observed for the FeTb alloy, where the Fe species is antiferromagnetically coupled with Tb atoms [79]. In this case the demagnetization pathway proceeds with two different timescales: a quick drop with a characteristic demagnetization time constant μ of 70 ± 20 fs, followed by slower dynamics and no evidence of recovery on the timescale of a few picoseconds. The analysis of the sample absorption time-dependent response is provided in Appendix C.

VI. CONCLUSION

The generation of highly coherent pulses in the water window (300–530 eV) and up to 790 eV has been successfully demonstrated by means of nonlinear harmonics generation from the FERMI seeded FEL. Our results demonstrate that the high coherence properties of the seed laser are transferred to both the fundamental FEL wavelength and its nonlinear harmonics. Foreshadowing the effective extension of the FERMI nominal spectral range to shorter wavelengths [80], we have demonstrated that nonlinear harmonics have performances comparable to standard fundamental emission in terms of wavelength stability, intensity fluctuation, and temporal jitter with respect to a passively synchronized optical laser. This paves the way for extending the class of experiments based on the simultaneous control and manipulation of both phase and wavelength in the soft-x-ray spectral range so far inaccessible for seeded FELs. In particular, recent theoretical [24] and experimental achievements [61] suggest that longitudinal coherence is a key parameter to modify the classical behavior of the Beer-Lambert law as a consequence of the directional behavior of stimulated emission. On a more general note, the concentration of a large number of coherent photons into a volume comparable to the one defined by their coherence properties, as well as their interaction with condensed matter [81–83], can induce the generation of light quantum states, for example, biphotons [84,85]. The latter could have important beneficial effects in diffraction-based imaging techniques, improving their resolution beyond the classical limit, or in the field of information technology. The high shot-by-shot stability of the pulse intensity and spectral properties exhibited by the nonlinear harmonics of FERMI, associated

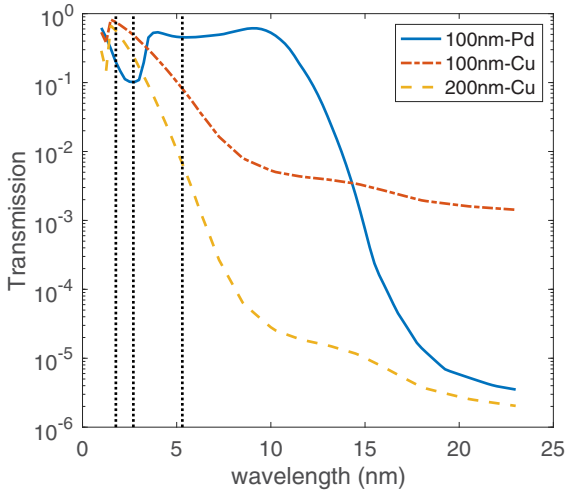

FIG. 11. Transmission curves of 100 nm Pd, 100 nm Cu, and 200 nm Cu in the spectral range of interest. The fundamental emission from the second stage (5.3 nm, i.e., 233 eV) and the second and third harmonics are highlighted by vertical dotted lines. (Data were taken from [89].)

with the remarkably low time jitter relative to the available user laser (a few femtoseconds) [71], can be employed in a wide class of single-shot pump-probe soft-x-ray spectroscopies. Furthermore, the FERMI FEL-2 scheme could lead to conduct EUV (fundamental) pump–soft-x-ray (harmonic) probe studies entering in the regime of linear or nonlinear multidimensional spectroscopy [86,87]. Indeed, combining coherence with the possibility to generate synchronized pulses of different wavelengths [88] enables a whole range of novel pump-probe experiments to investigate structural, electronic, and magnetization dynamics in the fields of condensed matter as well as atomic and molecular physics.

ACKNOWLEDGMENTS

The authors would like to thank the FERMI Team for support provided during the machine tuning and optimization of the FEL. The authors are grateful for financial support received from CNRS MOMENTUM and a LaserLab Europe users grant. Access to Synchrotron SOLEIL and beamline SEXTANTS through Proposal No. 20190664 for the characterization of static properties of the FeTb and CoPt thin films is acknowledged. Authors are in debt to Nicolas Jaouen and SEXTANTS beamline staff for the technical assistance during magnetic film characterization.

APPENDIX A: ESTIMATE OF THE FEL PULSE ENERGY AT ∼700 eV

To estimate the pulse energy at 700 eV, a calibrated photodiode and a set of three solid-state filters were used, i.e., a 100-nm-thick Pd filter, a 100-nm Cu filter, and a 200-nm Cu filter, whose transmission curves are reported in Fig. 11. The pulse energy measured by the photodiode is the sum of the pulse energy of all emitted wavelengths not completely cut by the filters. In the experimental configuration, the first HGHG stage was tuned at 21.2 nm and it was almost completely filtered out in all three conditions, so its contribution can be

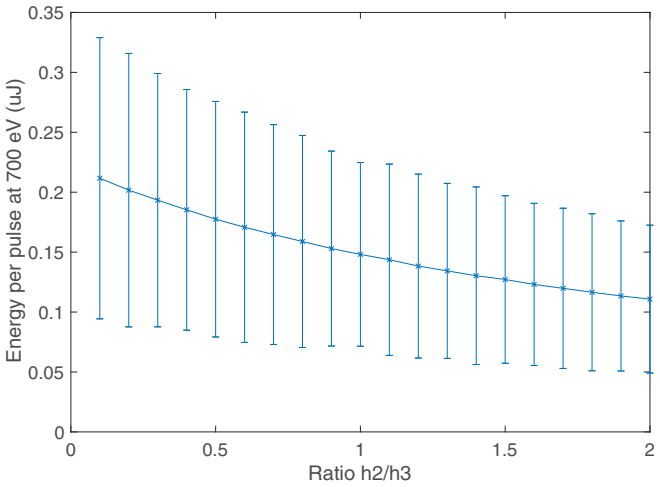

FIG. 12. Energy per pulse estimated at 700 eV as a function of the contribution of the second harmonic, ranging from 10% to a factor 2 of the third harmonic. Error bars are calculated assuming an uncertainty on the transmission coefficient of 2%–5%.

neglected. A series of single-shot pulse energy measurements in the three filtering conditions was taken. The intensity of the FEL is strongly dependent upon the electron bunch length in turn affected by the fluctuation of the machine parameters. For this reason, we recorded the shot-to-shot real-time measurement of the bunch length provided by a pyrodetector used in the bunch compression feedback and we filtered out all shots whose compression deviated by more than ±5%. The mean pulse energies measured in the three cases are 8.85 ± 0.61 μJ (100 nm Pd), 1.88 ± 0.26 μJ (100 nm Cu), and 0.185 ± 0.06 μJ (200 nm Cu).

We assume that the radiation collected by the photodiode mainly contained the fundamental of the second stage (5.3 nm, i.e., 233 eV) and its second and third harmonics, while higher harmonics can be neglected. The second harmonic is emitted off-axis and its contribution is of the same order of magnitude as the third harmonic, so it is not a completely independent parameter. We therefore consider the intensity of the fundamental and of the third harmonic as unknown variables and set the second harmonic intensity to a given fraction of the third (variable from 10% to a factor 2). In this way, the system of three equations in two unknowns can be solved with the least-squares method. We introduce a random error of 2%–5% on the transmission curve of Fig. 11, in order to take into account possible surface contamination of the filters. We obtain a mean pulse energy at the fundamental of about 19.4 μJ ± 0.1 μJ. Based on the contribution coming from the second harmonic, the pulse energy at the third harmonic varies from 210 nJ to 110 nJ with an uncertainty of about 50% as depicted in Fig. 12.

APPENDIX B: EXPERIMENTAL SETUP OF THE PUMP AND PROBE EXPERIMENT AT THE Co AND Fe $L_{2,3}$ edges

Figure 13 shows a sketch of the experimental setup designed to collect at the same time absorption and spin dynamics information of a magnetic sample using the amplification of nonlinear harmonic of the FERMI FEL-2 source.

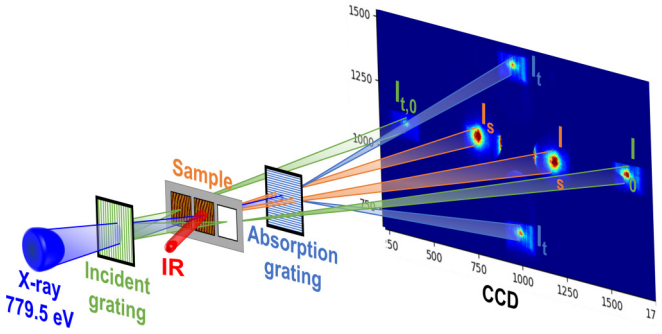

FIG. 13. Sketch of the experimental setup used to collect at the same time absorption and magnetic scattering information on FeTb and CoPt thin films.

In this scheme, the incident radiation is first dispersed in the horizontal plane by a 2×2 mm^2 grating. This grating (labeled "Incident grating" in Fig. 13) has a period of 80 nm, with a duty cycle of 25%, and has been realized by electron-beam nanolithography of a 30-nm-thick hydrogen silsesquioxane resist on Si_3N_4 membrane (250 nm thickness). In order to compensate for the different ratio between magnetically scattered photons and sample transmission, the grating efficiency is intentionally reduced below to 0.01%. This grating is mounted on a translation stage and one can tune the sample-to-grating distance from 120 to 180 mm. This distance is chosen in such a way that the beam separation between diffracted orders -1, 0, and $+1$ matches the 4-mm spacing of a multiarray window sample. One of these (labeled by I_0 in Fig. 13) passes through an empty membrane and is directly recorded on the CCD detector placed 300 mm after the sample, while the specular beam $I_{t,0}$ interacting with the thin-film membrane gives the static transmission of the sample. The zeroth order of the first grating impinges on a magnetic thin-film multilayer membrane which has magnetic stripe domains with out-of-plane magnetization.

This generates magnetically scattered photons I_s [90] that are recorded on the CCD plane. In order to determine the dynamical transmission of the film when the sample is pumped by an IR laser pulse, the transmitted beam is then diffracted by a second grating (80-nm pitch with structure similar to the first dispersive elements, labeled as "Absorption grating" in Fig. 13). This second grating is mounted on a second motorized translation stage at a sample-to-grating distance of 50 mm. The vertically scattered diffracted beams of this grating are recorded on the same CCD detector giving the dynamical transmission I_t of the pumped film. As discussed below, for each CCD picture we can extract once the time-dependent absorption $\mu = \ln(I_0/I_t)$, the static absorption $\mu_0 = \ln(I_0/I_{t,0})$, and the magnetization $M \propto \sqrt{I_s/I_0}$ as a function of the delay Δt between the pump and the probe or as a function of the probing energy. Figure 14 shows a typical example of the data acquired at the Co $L_{2,3}$ absorption edge of a CoPt multilayer film [Fig. 14(a)] and at the Fe edge of a FeTb sample [Fig. 14(b)]. In each CCD picture, the regions of interest (ROIs) taken for the CoPt sample [Fig. 14(a)] and FeTb [Fig. 14(b)], as well as a close-up of the different ROIs (circle or half circles), are shown from Fig. 14(c) to Fig. 14(n). The intensities are retrieved by taking the mean

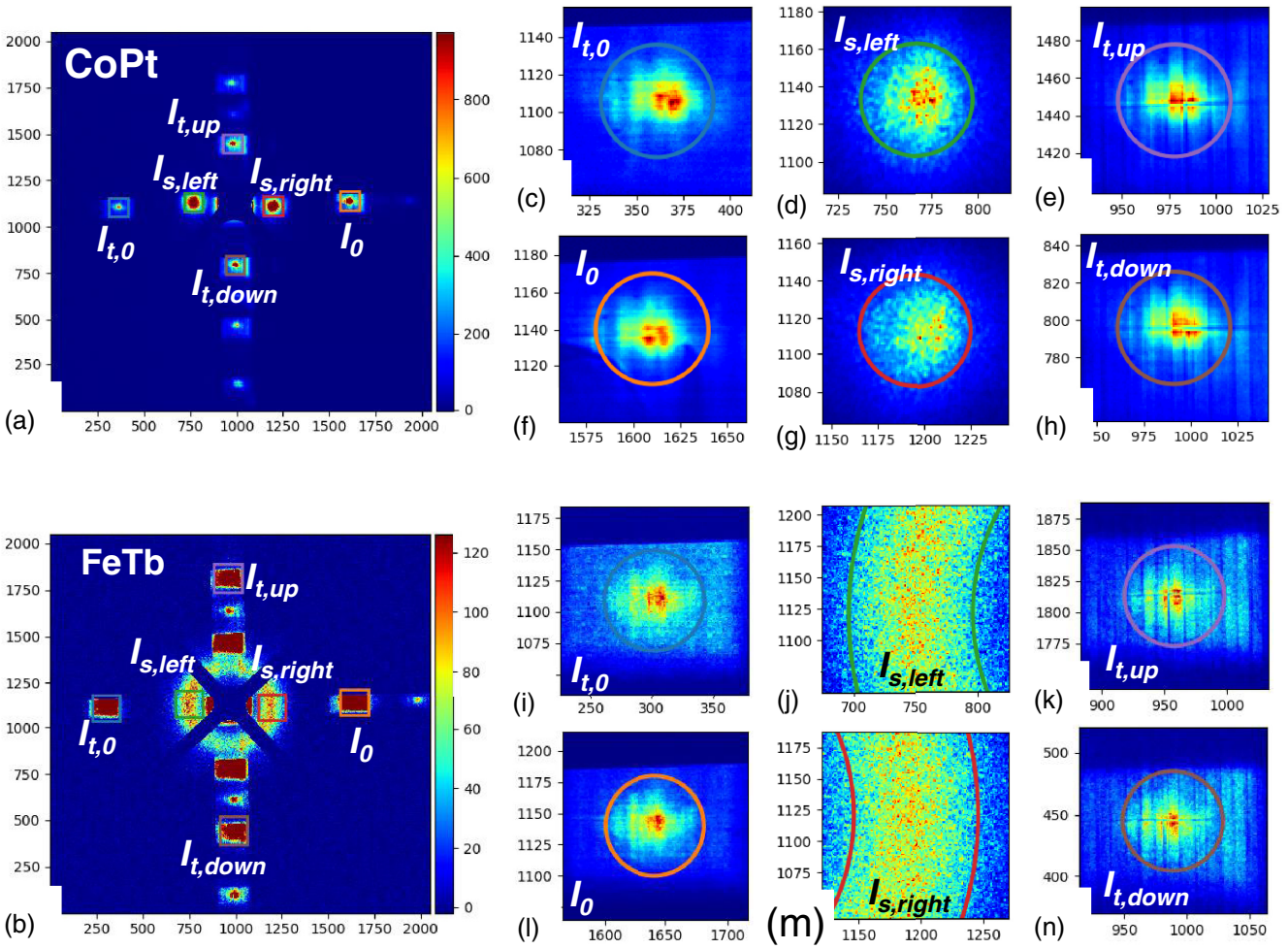

FIG. 14. Examples of typical recorded images on (a) CoPt and (b) FeTb samples. The squares inside the images highlight the different ROIs signals with the convention described in the main text. ROIs from (c) to (h) for the CoPt sample and from (i) to (n) for FeTb show the different diffraction spots used to retrieve the information for the static absorption μ_0, the dynamic absorption μ, and the magnetic signal M. Additional diffraction orders visible in the images are due to the contamination of low-energy photons produced by the source.

values inside the marked ROIs in Figs. 14(c)–14(e) for CoPt and in Figs. 14(i)–14(n) for FeTb. Then I_s right and left as well as I_t up and down are averaged, so for each CCD picture, four different quantities I_0, $I_{t,0}$, I_s, and I_t are extracted. For FeTb, $I_{t,\mathrm{up}}$ and $I_{t,\mathrm{down}}$ are taken from the second order of diffraction to avoid any overlap with the magnetic scattering which is almost ringlike. The less intense spots in the vertical middle line between the first and the second order of the absorption grating are the diffraction by this grating of the second harmonic of the FEL beam, while the first order is blocked by upstream filters as previously described.

In order to assess the spectroscopic capability of the nonlinear high-order harmonics produced by the FERMI seeded FEL, Fig. 15 displays the XAS spectrum taken at the Fe L_3 edge, using the above-described analysis method to reduce the data, with an energy scan taken on the same sample at the SEXTANTS beamline of the SOLEIL synchrotron radiation source [91]. Figure 15 shows that the experimental absorption spectrum obtained by scanning the FEL emission from 702 eV to 716 eV can be reproduced from synchrotron radiation data by applying a Gaussian convolution of 0.8 eV FWHM.

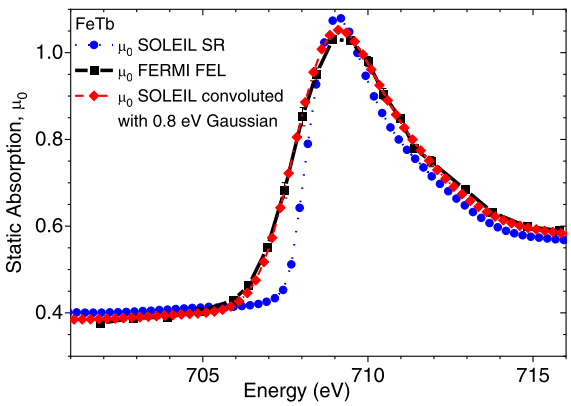

FIG. 15. Static absorption measured at the SOLEIL synchrotron (blue circles) and averaged static absorption measured at FERMI (black squares) for the same FeTb sample with the identical magnetization state (aligned magnetic domains out of plane). FERMI static absorption can be retrieved from SOLEIL static absorption and a convolution with a Gaussian having a FWHM of 0.8 eV (red diamonds).

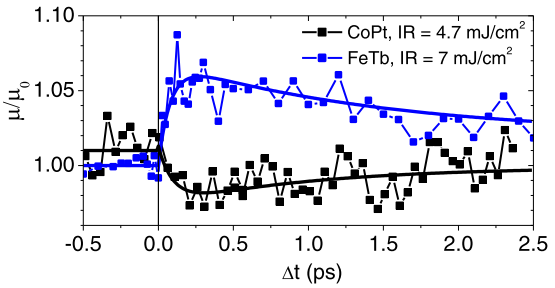

FIG. 16. Relative absorption as a function of the time delay for CoPt [778.5 eV, black (dark gray)] and FeTb strongly pumped [707.5 eV, blue (light gray)]. XAS dynamics can be observed when the pump is sufficiently intense, due to a redshift of the absorption spectrum maximum [92].

The obtained energy resolution $\Delta E/E$ of about 1.1×10^{-3} is consistent with the average spectral properties of the source described in the main text.

APPENDIX C: ANALYSIS OF THE FeTb AND CoPt XAS TIME-DEPENDENT RESPONSE TO THE IR PUMP

In order to compare the time-dependent sample response, Fig. 16 shows the dynamics at a given probing photon energy for the two samples. The data report the relative absorption μ/μ_0 for FeTb (707.5 eV, blue) and CoPt (778.5 eV, black). We observe that, with increasing IR laser fluence with respect to the energy scan reported in Fig. 10, the absorption signal of the FeTb film is more sensitive to the optical excitation. The response of the absorption signal is different for the two samples: While FeTb shows an increase of sample absorption after t_0, a reduction is observed for the CoPt film. We ascribe this behavior to a difference in probing photon energy with respect to the material absorption edge. Indeed, pumping with 1.5-eV photons changes the electronic density of state close to the Fermi energy and according to Carva *et al.* [92] this produces a dynamical shift of the XAS spectrum toward lower energy, opening new available states for the transition from a core level to the conduction band. For the 707.5-eV photons used to probe Fe in the FeTb sample, they are 1.5 eV below the maximum sample absorption (709 eV, Fig. 15); as a consequence, after the optical excitation this produces an increase of sample absorption. On the other hand, for CoPt, the probing energy is closer to the absorption peak (779.5 eV), so a 1.5 eV optical excitation results in a decrease of the available states above the conduction band for 778.5-eV photons, producing a decrease of sample absorption. A similar dependence of the XAS response on the relative detuning of the probing photon energy from the resonance condition has been reported recently on transition metal samples at $M_{3,2}$ edges [93,94].

[1] C. Pellegrini, A. Marinelli, and S. Reiche, The physics of x-ray free-electron lasers, Rev. Mod. Phys. **88**, 015006 (2016).

[2] L. H. Yu, Generation of intense uv radiation by subharmonically seeded single-pass free-electron lasers, Phys. Rev. A **44**, 5178 (1991).

[3] J. M. Madey, Stimulated emission of bremsstrahlung in a periodic magnetic field, J. Appl. Phys. **42**, 1906 (1971).

[4] L.-H. Yu, M. Babzien I. Ben-Zvi, L. F. DiMauro, A. Doyuran, W. Graves, E. Johnson, S. Krinsky, R. Malone, I. Pogorelsky *et al.*, High-gain harmonic-generation free-electron laser, Science **289**, 932 (2000).

[5] G. De Ninno, D. Gauthier, B. Mahieu, P. R. Ribič, E. Allaria, P. Cinquegrana, M. B. Danailov, A. Demidovich, E. Ferrari, L. Giannessi, G. Penco, P. Sigalotti, and M. Stupar, Single-shot spectro-temporal characterization of XUV pulses from a seeded free-electron laser, Nat. Commun. **6**, 8075 (2015).

[6] D. Gauthier, P. R. Ribič, G. De Ninno, E. Allaria, P. Cinquegrana, M. B. Danailov, A. Demidovich, E. Ferrari, L. Giannessi, B. Mahieu, and G. Penco, Spectrotemporal Shaping of Seeded Free-Electron Laser Pulses, Phys. Rev. Lett. **115**, 114801 (2015).

[7] E. Allaria and G. De Ninno, Soft-X-Ray Coherent Radiation Using a Single-Cascade Free-Electron Laser, Phys. Rev. Lett. **99**, 014801 (2007).

[8] A. M. Kondratenko and E. L. Saldin, Generation of coherent radiation by a relativistic electron beam in an undulator, Partic. Accel. **10**, 207 (1980).

[9] P. Sprangle, C.-M. Tang, and W. M. Manheimer, Nonlinear theory of free-electron lasers and efficiency enhancement, Phys. Rev. A **21**, 302 (1980).

[10] R. Bonifacio, C. Pellegrini, and L. M. Narducci, Collective instabilities and high-gain regime in a free-electron laser, Opt. Commun. **50**, 373 (1984).

[11] G. Penco, G. Perosa, E. Allaria, S. Di Mitri, E. Ferrari, L. Giannessi, S. Spampinati, C. Spezzani, and M. Veronese, Enhanced seeded free electron laser performance with a "cold" electron beam, Phys. Rev. Accel. Beams **23**, 120704 (2020).

[12] R. K. Lam, S. L. Raj, T. A. Pascal, C. D. Pemmaraju, L. Foglia, A. Simoncig, N. Fabris, P. Miotti, C. J. Hull, A. M. Rizzuto *et al.*, Soft X-Ray Second Harmonic Generation as an Interfacial Probe, Phys. Rev. Lett. **120**, 023901 (2018).

[13] H.-Y. Wang, S. Schreck, M. Weston, C. Liu, H. Ogasawara, J. LaRue, F. Perakis, M. Dell'Angela, F. Capotondi, L. Gianessi *et al.*, Time-resolved observation of transient precursor state of CO on Ru(0001) using carbon K-edge spectroscopy, Phys. Chem. Chem. Phys. **22**, 2677 (2020).

[14] E. Diesen, H.-Y. Wang, S. Schreck, M. Weston, H. Ogasawara, J. LaRue, F. Perakis, M. Dell'Angela, F. Capotondi, L. Giannessi *et al.*, Ultrafast Adsorbate Excitation Probed with Subpicosecond-Resolution X-Ray Absorption Spectroscopy, Phys. Rev. Lett. **127**, 016802 (2021).

[15] E. Allaria, D. Castronovo, P. Cinquegrana, P. Craievich, M. Dal Forno, M. B. Danailov, G. D'Auria, A. Demidovich, G. De Ninno, S. Di Mitri *et al.*, Two-stage seeded soft-X-ray free-electron laser, Nat. Photon. **7**, 913 (2013).

[16] E. Allaria, L. Badano, S. Bassanese, F. Capotondi, D. Castronovo, P. Cinquegrana, M. B. Danailov, G. D'Auria, A. Demidovich, R. De Monte *et al.*, The FERMI free-electron lasers, J. Synchrotron Radiat. **22**, 485 (2015).

[17] G. Stupakov, Using the Beam-Echo Effect for Generation of Short-Wavelength Radiation, Phys. Rev. Lett. **102**, 074801 (2009).

[18] D. Xiang, E. Colby, M. Dunning, S. Gilevich, C. Hast, K. Jobe, D. McCormick, J. Nelson, T. O. Raubenheimer, K. Soong, G. Stupakov, Z. Szalata, D. Walz, S. Weathersby, M. Woodley, and P.-L. Pernet, Demonstration of the Echo-Enabled Harmonic Generation Technique for Short-Wavelength Seeded Free Electron Lasers, Phys. Rev. Lett. **105**, 114801 (2010).

[19] P. R. Ribič, A. Abrami, L. Badano, M. Bossi, H.-H. Braun, N. Bruchon, F. Capotondi, D. Castronovo, M. Cautero, P. Cinquegrana *et al.*, Coherent soft X-ray pulses from an echo-enabled harmonic generation free-electron laser, Nat. Photon. **13**, 555 (2019).

[20] E. Hemsing, G. Marcus, W. M. Fawley, R. W. Schoenlein, R. Coffee, G. Dakovski, J. Hastings, Z. Huang, D. Ratner, T. Raubenheimer, and G. Penn, Soft x-ray seeding studies for the SLAC Linac Coherent Light Source II, Phys. Rev. Accel. Beams **22**, 110701 (2019).

[21] K. Zhang, T. Liu, Z. Qi, X. Fu, C. Feng, H. Deng, and B. Liu, Extending the photon energy coverage of a seeded free-electron laser via reverse taper enhanced harmonic cascade, Photonics **8**, 44 (2021).

[22] FERMI FEL 2.0 Conceptual Design Report, available at https://www.elettra.trieste.it/images/Documents/FERMI%20Machine/Machine/CDR/FERMI2.0CDR.pdf (unpublished).

[23] T. Wang, D. Zhu, B. Wu, C. Graves, S. Schaffert, T. Rander, L. Müller, B. Vodungbo, C. Baumier, D. P. Bernstein *et al.*, Femtosecond Single-Shot Imaging of Nanoscale Ferromagnetic Order in Co/Pd Multilayers Using Resonant X-Ray Holography Phys. Rev. Lett. **108**, 267403 (2012).

[24] J. Stöhr and A. Scherz, Creation of X-Ray Transparency of Matter by Stimulated Elastic Forward Scattering, Phys. Rev. Lett. **115**, 107402 (2015).

[25] D. J. Higley, A. H. Reid, Z. Chen, L. Le Guyader, O. Hellwig, A. A. Lutman, T. Liu, P. Shafer, T. Chase, G. L. Dakovski, A. Mitra, E. Yuan, J. Schlappa, H. A. Dürr, W. F. Schlotter, and J. Stöhr, Femtosecond X-ray induced changes of the electronic and magnetic response of solids from electron redistribution, Nat. Commun. **10**, 5289 (2019).

[26] S. Corby, R. R. Rao, L. Steier, and J. R. Durrant, The kinetics of metal oxide photoanodes from charge generation to catalysis, Nat. Rev. Mater. **6**, 1136 (2021).

[27] K. H. Kim, K. Amann-Winkel, N. Giovambattista, A. Späh, F. Perakis, H. Pathak, M. L. Parada, C. Yang, D. Mariedahl, T. Eklund *et al.*, Experimental observation of the liquid-liquid transition in bulk supercooled water under pressure, Science **370**, 978 (2020).

[28] J. B. Murphy, C. Pellegrini, and R. Bonifacio, Collective instability of a free electron laser including space charge and harmonics, Optics Commun. **53**, 197 (1985).

[29] Z. Huang and K.-J. Kim, Three-dimensional analysis of harmonic generation in high-gain free-electron lasers, Phys. Rev. E **62**, 7295 (2000).

[30] A. Tremaine, X. J. Wang, M. Babzien, I. Ben-Zvi, M. Cornacchia, H.-D. Nuhn, R. Malone, A. Murokh, C. Pellegrini, S. Reiche, J. Rosenzweig, and V. Yakimenko, Experimental Characterization of Nonlinear Harmonic Radiation from a Visible Self-Amplified Spontaneous Emission Free-Electron Laser at Saturation, Phys. Rev. Lett. **88**, 204801 (2002).

[31] E. L. Saldin, E. A. Schneidmiller, and M. V. Yurkov, Properties of the third harmonic of the radiation from self-amplified spontaneous emission free electron laser Phys. Rev. ST Accel. Beams **9**, 030702 (2006)

[32] H. P. Freund, S. G. Biedron, and S. V. Milton, Nonlinear harmonic generation and proposed experimental verification in SASE FELs, Nucl. Instrum. Methods Phys. Res. Sect. A **445**, 53 (2000).

[33] M. Abo-Bakr, K. Goldammer, T. Kamps, J. Knobloch, B. Kuske, T. Leitner, and A. Meseck, Nonlinear harmonic generation in the STARS FEL, Nucl. Instrum. Methods Phys. Res. Sect. A **593**, 6 (2008).

[34] D. Ratner, A. Brachmann, F. J. Decker, Y. Ding, D. Dowell, P. Emma, A. Fisher, J. Frisch, S. Gilevich, Z. Huang *et al.*, Second and third harmonic measurements at the linac coherent light source, Phys. Rev. ST Accel. Beams **14**, 060701 (2011).

[35] B. W. J. McNeil, G. R. M. Robb, M. W. Poole, and N. R. Thompson, Harmonic Lasing in a Free-Electron-Laser Amplifier, Phys. Rev. Lett. **96**, 084801 (2006).

[36] E. A. Schneidmiller and M. V. Yurkov, Harmonic lasing in x-ray free electron lasers, Phys. Rev. ST Accel. Beams **15**, 080702 (2012).

[37] E. A. Schneidmiller, F. Brinker, W. Decking, L. Froehlich, M. Guetg, D. Noelle, M. Scholz, M. V. Yurkov, I. Zagorodnov, G. Geloni *et al.*, Observation of harmonic lasing in the Angstrom regime at European X-ray Free Electron Laser, Phys. Rev. Accel. Beams **24**, 030701 (2021).

[38] I. Nama, C.-K. Min, C. Kim, H. Yang, G. Kim, H. Heo, S. Kwon, S. H. Park, and H.-S. Kang, Soft X-ray harmonic lasing self-seeded free electron laser at Pohang Accelerator Laboratory X-ray free electron laser, Appl. Phys. Lett. **112**, 213506 (2018).

[39] D. Ratner, R. Abela, J. Amann, C. Behrens, D. Bohler, G. Bouchard, C. Bostedt, M. Boyes, K. Chow, D. Cocco *et al.*, Experimental Demonstration of a Soft X-Ray Self-Seeded Free-Electron Laser, Phys. Rev. Lett. **114**, 054801 (2015).

[40] J. Amann, W. Berg, V. Blank, F.-J. Decker, Y. Ding, P. Emma, Y. Feng, J. Frisch, D. Fritz, J. Hastings *et al.*, Demonstration of self-seeding in a hard-X-ray free-electron laser, Nat. Photon. **6**, 693 (2012).

[41] I. Nam, C.-K. Min, B. Oh, G. Kim, D. Na, Y. J. Suh, H. Yang, M. H. Cho, C. Kim, M.-J. Kim *et al.*, High-brightness self-seeded X-ray free-electron laser covering the 3.5 keV to 14.6 keV range, Nat. Photon. **15**, 435 (2021).

[42] I. A. Vartanyants (private communication).

[43] C. Dornes, Y. Acremann, M. Savoini, M. Kubli, M. J. Neugebauer, E. Abreu, L. Huber, G. Lantz, C. A. F. Vaz, H. Lemke *et al.*, The ultrafast Einstein–de Haas effect, Nature (London) **565**, 209 (2019).

[44] L. Shen, M. Seaberg, E. Blackburn, and J. J. Turner, A snapshot review—Fluctuations in quantum materials: From skyrmions to superconductivity, MRS Adv. **6**, 221 (2021).

[45] K. J. Gaffney, Capturing photochemical and photophysical transformations in iron complexes with ultrafast X-ray spectroscopy and scattering, Chem. Sci. **12**, 8010 (2021).

[46] E. Allaria, R. Appio, L. Badano, W. A. Barletta, S. Bassanese, S. G. Biedron, A. Borga, E. Busetto, D. Castronovo, P. Cinquegrana *et al.*, Highly coherent and stable pulses from the FERMI seeded free-electron laser in the extreme ultraviolet, Nat. Photon. **6**, 699 (2012).

[47] I. Ben-Zvi, K. M. Yang, and L. H. Yu, The fresh-bunch technique in FELs, Nucl. Instrum. Methods Phys. Res. Sect. A **318**, 726 (1992).

[48] H. Wang, P. Bencok, P. Steadman, E. Longhi, J. Zhu, and Z. Wang, Complete polarization analysis of an APPLE II undulator using a soft X-ray polarimeter, J. Synchrotron Radiat. **19**, 944 (2012).

[49] E. Allaria, B. Diviacco, C. Callegari, P. Finetti, B. Mahieu, J. Viefhaus, M. Zangrando, G. De Ninno, G. Lambert, E. Ferrari *et al.*, Control of the Polarization of a Vacuum-Ultraviolet, High-Gain, Free-Electron Laser, Phys. Rev. X **4**, 041040 (2014).

[50] E. Allaria, F. Curbis, M. Coreno, M. Danailov, B. Diviacco, C. Spezzani, M. Trovó, and G. De Ninno, Experimental Characterization of Nonlinear Harmonic Generation in Planar and Helical Undulators, Phys. Rev. Lett. **100**, 174801 (2008).

[51] C. Spezzani, E. Allaria, M. Coreno, B. Diviacco, E. Ferrari, G. Geloni, E. Karantzoulis, B. Mahieu, M. Vento, and G. De Ninno, Coherent Light with Tunable Polarization from Single-Pass Free-Electron Lasers, Phys. Rev. Lett. **107**, 084801 (2011).

[52] E. Allaria, G. De Ninno, G. Geloni, and C. Spezzani, Angular distribution of nonlinear harmonic generation in helical undulators: A comparison between experiments and theory, Nucl. Instrum. Methods Phys. Res. Sect. A **654**, 575 (2011).

[53] C. Svetina, D. Cocco, N. Mahne, L. Raimondi, E. Ferrari, and M. Zangrando, PRESTO, the on-line photon energy spectrometer at FERMI: Design, features and commissioning results, J. Synchrotron Radiat. **23**, 35 (2016).

[54] M. Zangrando, A. Abrami, D. Bacescu, I. Cudin, C. Fava, F. Frassetto, A. Galimberti, R. Godnig, D. Giuressi, L. Poletto, L. Rumiz, R. Sergo, C. Svetina, and D. Cocco, The photon analysis, delivery, and reduction system at the FERMI@Elettra free electron laser user facility, Rev. Sci. Instrum. **80**, 113110 (2009).

[55] C. Ferrante, E. Principi, A. Marini, G. Batignani, G. Fumero, A. Virga, L. Foglia, R. Mincigrucci, A. Simoncig, C. Spezzani, C. Masciovecchio, and T. Scopigno, Non-linear self-driven spectral tuning of extreme ultraviolet femtosecond pulses in monoatomic materials, Light Sci. Appl. **10**, 92 (2021).

[56] S. Reiche, Nucl. Instrum. Methods Phys. Res. Sect. A **429**, 243 (1999).

[57] Z. Huang, M. Borland, P. Emma, J. Wu, C. Limborg, G. Stupakov, and J. Welch, Suppression of microbunching instability in the linac coherent light source, Phys. Rev. ST Accel. Beams **7**, 074401 (2004).

[58] S. Di Mitri and S. Spampinati, Microbunching instability study in a linac-driven free electron laser spreader beam line, Phys. Rev. Accel. Beams **20**, 120701 (2017).

[59] S. Spampinati, E. Allaria, L. Badano, S. Bassanese, S. Biedron, D. Castronovo, P. Craievich, M. B. Danailov, A. Demidovich, G. De Ninno *et al.*, Laser heater commissioning at an externally seeded free-electron laser, Phys. Rev. ST Accel. Beams **17**, 120705 (2014).

[60] G. Perosa, E. M. Allaria, L. Badano, N. Bruchon, P. Cinquegrana, M. B. Danailov, A. Demidovich, G. De Ninno, L. Giannessi, N. Mirian, G. M. Penco, P. Rebernik, E. Roussel, P. Sigalotti, S. Spampinati, M. Veronese, M. Trovò, and S. Di Mitri, Linear optics control of sideband instability for improved free-electron laser spectral brightness, Phys. Rev. Accel. Beams **23**, 110703 (2020).

[61] B. Wu, T. Wang, C. E. Graves, D. Zhu, W. F. Schlotter, J. J. Turner, O. Hellwig, Z. Chen, H. A. Dürr, A. Scherz, and J. Stöhr, Elimination of X-Ray Diffraction through Stimulated X-Ray Transmission, Phys. Rev. Lett. **117**, 027401 (2016).

[62] O. Y. Gorobtsov, G. Mercurio, G. Brenner, U. Lorenz, N. Gerasimova, R. P. Kurta, F. Hieke, P. Skopintsev, I. Zaluzhnyy, S. Lazarev, D. Dzhigaev, M. Rose, A. Singer, W. Wurth, and I. A. Vartanyants, Statistical properties of a free-electron laser revealed by Hanbury Brown–Twiss interferometry, Phys. Rev. A **95**, 023843 (2017).

[63] O. Y. Gorobtsov, G. Mercurio, F. Capotondi, P. Skopintsev, S. Lazarev, I. A. Zaluzhnyy, M. B. Danailov, M. Dell'Angela, M. Manfredda, E. Pedersoli, L. Giannessi, M. Kiskinova, K. C. Prince, W. Wurth, and I. A. Vartanyants, Seeded X-ray free-electron laser generating radiation with laser statistical properties, Nat. Commun. **9**, 4498 (2018).

[64] E. L. Saldin, E. A. Schneidmiller, and M. V. Yurkov, Study of a noise degradation of amplification process in a multistage HGHG FEL, Opt. Commun. **202**, 169 (2002).

[65] R. Loudon, *The Quantum Theory of Light*, 3rd ed. (Oxford University Press, Oxford, 2000).

[66] A. A. Lutman, Y. Ding, Y. Feng, Z. Huang, M. Messerschmidt, J. Wu, and J. Krzywinski, Femtosecond x-ray free electron laser pulse duration measurement from spectral correlation function, Phys. Rev. ST Accel. Beams **15**, 030705 (2012).

[67] Y. Inubushi, K. Tono, T. Togashi, T. Sato, T. Hatsui, T. Kameshima, K. Togawa, T. Hara, T. Tanaka, H. Tanaka, T. Ishikawa, and M. Yabashi, Determination of the Pulse Duration of an X-Ray Free Electron Laser Using Highly Resolved Single-Shot Spectra, Phys. Rev. Lett. **109**, 144801 (2012).

[68] A. Singer, U. Lorenz, F. Sorgenfrei, N. Gerasimova, J. Gulden, O. M. Yefanov, R. P. Kurta, A. Shabalin, R. Dronyak, R. Treusch, V. Kocharyan, E. Weckert, W. Wurth, and I. A. Vartanyants, Hanbury Brown–Twiss Interferometry at a Free-Electron Laser, Phys. Rev. Lett. **111**, 034802 (2013).

[69] L-A. Näslund, J. Lüning, Y. Ufuktepe, H. Ogasawara, P. Wernet, U. Bergmann, L. G. M. Pettersson, and A. Nilsson, X-ray absorption spectroscopy measurements of liquid water, J. Phys. Chem. B **109**, 13835 (2005).

[70] M. B. Danailov, A. Demidovich, R. Ivanov, I. Nikolov, P. Sigalotti, and P. Cinquegrana, in *Proceedings of the 33rd International Free Electron Laser Conference, Shanghai, 2011*, edited by Z. Zhao and D. Wang (Shanghai Institute of Applied Physics, Shanghai, 2012), paper TUOC4.

[71] P. Cinquegrana, A. Demidovich, G. Kurdi, I. Nikolov, P. Sigalotti, P. Susnjar, and M. B. Danailov, The seed laser system of the FERMI free-electron laser: Design, performance and near future upgrades, High Power Laser Sci. Eng. **9**, e61 (2021).

[72] F. Capotondi, E. Pedersoli, F. Bencivenga, M. Manfredda, N. Mahne, L. Raimondi, C. Svetina, M. Zangrando, A. Demidovich, I. Nikolov, M. Danailov, C. Masciovecchio, and M. Kiskinova, Multipurpose end-station for coherent diffraction imaging and scattering at FERMI@Elettra free-electron laser facility, J. Synchrotron Radiat. **22**, 544 (2015).

[73] F. Capotondi, E. Pedersoli, N. Mahne, R. H. Menk, G. Passos, L. Raimondi, C. Svetina, G. Sandrin, M. Zangrando, M. Kiskinova *et al.*, Coherent imaging using seeded free-electron laser pulses with variable polarization: First results and research opportunities, Rev. Sci. Instrum. **84**, 051301 (2013).

[74] T. Kachel, K. Holldack, S. Khan, R. Mitzner, T. Quast, C. Stamm, and H. A. Duerr, in *Proceedings of the Ninth International Conference on Synchrotron Radiation Instrumentation, Daegu, 2006*, edited by J.-Y. Choi and S. Rah, *AIP Conf. Proc. No.* 879 (AIP, Melville, 2007), p. 1250.

[75] P. Prigent, P. Hollander, M. Labat, M. E. Couprie, J. L. Marlats, C. Laulhé, J. Luning, T. Moreno, P. Morin, A. Nadji, F. Polack, S. Ravy, M. Silly, and F. Sirotti, Progress on the Femto-Slicing project at the synchrotron SOLEIL, J. Phys.: Conf. Ser. **425**, 072022 (2013).

[76] B. Vodungbo, B. Tudu, J. Perron, R. Delaunay, L. Müller, M. H. Berntsen, G. Grübel, G. Malinowski, C. Weier, J. Gautier *et al.*, Indirect excitation of ultrafast demagnetization, Sci. Rep. **6**, 18970 (2016).

[77] N. Moisan, G. Malinowski, J. Mauchain, M. Hehn, B. Vodungbo, J. Lüning, S. Mangin, E. E. Fullerton, and A. Thiaville, Investigating the role of superdiffusive currents in laser induced demagnetization of ferromagnets with nanoscale magnetic domains, Sci. Rep. **4**, 4658 (2015).

[78] I. Vaskivskyi, R. S. Malik, L. Salemi, D. Turenne, R. Knut, J. Brock, R. Stefanuik, J. Söderström, K. Carva, E. E. Fullerton, P. M. Oppeneer, O. Karis, and H. A. Dürr, Element-specific magnetization dynamics in CoPt alloys induced by strong optical excitation, J. Phys. Chem. C **125**, 11714 (2021).

[79] A. R. Khorsand, M. Savoini, A. Kirilyuk, A. V. Kimel, A. Tsukamoto, A. Itoh, and T. Rasing, Element-Specific Probing of Ultrafast Spin Dynamics in Multisublattice Magnets with Visible Light, Phys. Rev. Lett. **110**, 107205 (2013).

[80] CDR FERMI 2.

[81] J. Stöhr, Two-Photon X-Ray Diffraction, Phys. Rev. Lett. **118**, 024801 (2017).

[82] J. Stöhr, Overcoming the diffraction limit by multi-photon interference: A tutorial, Adv. Opt. Photon. **11**, 215 (2019).

[83] S. Mukamel, M. Freyberger, W. Schleich, M. Bellini, A. Zavatta, G. Leuchs, C. Silberhorn, R. W. Boyd, L. L. Sánchez-Soto, A. Stefanov *et al.*, Roadmap on quantum light spectroscopy, J. Phys. B **53**, 072002 (2020).

[84] J. Stöhr, Diffraction without waves: Emergence of the quantum substructure of light, arXiv:2003.14217v1.

[85] Z. Chen, D. J. Higley, M. Beye, M. Hantschmann, V. Mehta, O. Hellwig, A. Mitra, S. Bonetti, M. Bucher, S. Carron, T. Chase, E. Jal, R. Kukreja, T. Liu, A. H. Reid, G. L. Dakovski, A. Föhlisch, W. F. Schlotter, H. A. Dürr, and J. Stöhr, Ultrafast Self-Induced X-Ray Transparency and Loss of Magnetic Diffraction, Phys. Rev. Lett. **121**, 137403 (2018).

[86] K. Bennett, Y. Zhang, M. Kowalewski, W. Hua, and S. Mukamel, Multidimensional resonant nonlinear spectroscopy with coherent broadband x-ray pulses, Phys. Scr. **T169**, 014002 (2016).

[87] M. Kowalewski, B. P. Fingerhut, K. E. Dorfman, K. Bennett, and S. Mukamel, Simulating coherent multidimensional spectroscopy of nonadiabatic molecular processes: From the infrared to the x-ray regime, Chem. Rev. **117**, 12165 (2017).

[88] E. Ferrari, C. Spezzani, F. Fortuna, R. Delaunay, F. Vidal, I. Nikolov, P. Cinquegrana, B. Diviacco, D. Gauthier, G. Penco *et al.*, Widely tunable two-colour seeded free-electron laser source for resonant-pump resonant-probe magnetic scattering, Nat. Commun. **7**, 10343 (2016).

[89] B. L. Henke, E. M. Gullikson, and J. C. Davis, photoabsorption, scattering, transmission, and reflection at $E =$ 50-30,000 eV, $Z =$ 1-92, At. Data Nucl. Data Tables **54**, 181 (1993).

[90] B. Vodungbo, J. Gautier, G. Lambert, A. B. Sardinha, M. Lozano, S. Sebban, M. Ducousso, W. Boutu, K. Li, B. Tudu, M. Tortarolo, R. Hawaldar, R. Delaunay, V. López-Flores, J. Arabski, C. Boeglin, H. Merdji, P. Zeitoun, and J. Lüning, Laser-induced ultrafast demagnetization in the presence of a nanoscale magnetic domain network, Nat. Commun. **3**, 999 (2012)

[91] M. Sacchi, N. Jaouen, H. Popescu, R. Gaudemer, J. M. Tonnerre, S. G. Chiuzbaian, C. F. Hague, A. Delmotte, J. M. Dubuisson, G. Cauchon, B. Lagarde, and F. Polack, The SEXTANTS beamline at SOLEIL: A new facility for elastic, inelastic and coherent scattering of soft X-rays, J. Phys.: Conf. Ser. **425**, 072018 (2013).

[92] K. Carva, D. Legut, and P. M. Oppeneer, Influence of laser-excited electron distributions on the X-ray magnetic circular dichroism spectra: Implications for femtosecond demagnetization in Ni Europhys. Lett. **86**, 57002 (2009).

[93] B. Rösner, B. Vodungbo, V. Chardonnet, F. Döring, V. A. Guzenko, M. Hennes, A. Kleibert, M. Lebugle, J. Lüning, N. Mahne *et al.*, Simultaneous two-color snapshot view on ultrafast charge and spin dynamics in a Fe-Cu-Ni tri-layer, Struct. Dyn. **7**, 054302 (2020).

[94] M. Hennes, B. Rösner, V. Chardonnet, G. S. Chiuzbaian, R. Delaunay, F. Döring, V. A. Guzenko, M. Hehn, R. Jarrier, A. Kleibert *et al.*, Time-resolved XUV absorption spectroscopy and magnetic circular dichroism at the Ni $M_{2,3}$-edges, Appl. Sci. **11**, 325 (2021).